Engineering Photon-Photon Interactions within Rubidium-filled Waveguides

C. Perrella,[1] P. S. Light,[1] S. Afshar Vahid,[2] F. Benabid,[3] and A. N. Luiten[1]

[1] *Institute for Photonics and Advanced Sensing (IPAS) and the School of Physical Sciences, The University of Adelaide, Adelaide, Australia*

[2] *Laser Physics and Photonic Devices Laboratories, School of Engineering, The University of South Australia, Adelaide, Australia*

[3] *GPPMM group, Xlim Research Institute, CNRS UMR 7252, Universite de Limoges, France*

Strong photon-photon interactions are a required ingredient for deterministic two-photon optical quantum logic gates. Multi-photon transitions in dense atomic vapors have been shown to be a promising avenue for producing such interactions. The strength of a multi-photon interaction can be enhanced by conducting the interaction in highly confined geometries such as small cross-section optical waveguides. Here we demonstrate, both experimentally and theoretically, that the strength of such interactions only scale with the optical mode diameter, d, not d^2 as might be initially expected. This weakening of the interaction arises from atomic motion inside the waveguides. We create an interaction between two optical signals at 780 nm and 776 nm using the $5S_{1/2}\rightarrow 5D_{5/2}$ two-photon transition in Rubidium vapor within a range of hollow-core fibers with different core sizes. The interaction strength was characterized by observing the absorption and phase shift induced on the 780 nm beam which is in close agreement with theoretical modeling that accounts for the atomic motion inside the fibers. This demonstrates that transit-time effects upon multi-photon transitions are of key importance when engineering photon-photon interactions within small cross-section waveguides that might otherwise be thought to lead to enhanced optical non-linearity through increased intensities.

I. INTRODUCTION

Photons are an attractive candidate for quantum computation [1, 2] because of their inherently high degree of environmental isolation. However, this key advantage leads directly to their greatest downside, an inherent difficulty in producing controllable and large interactions between two individual photons [1, 2]. One area of active research that aims to overcome this downside is the use of multi-photon transitions in atomic vapors that have been shown to act as an excellent mediator for generating strong photon-photon interactions [3]. This is particularly the case if these interactions can be performed in constrained geometries, which intrinsically enhance the intensity of the photon beams.

The threshold required for deterministic photon processing is the production of a 10^{-5} to 10^{-2} radian optical phase shift as a result of a single photon-photon interaction [4–6]. To reach such a target, enhancement of the photon-photon interaction strength can be created by performing the photon-atom interaction inside small cross-section and low-loss engineered waveguides. A number of experimental approaches using warm atomic vapors on different platforms have been made using this philosophy including: hollow-core photonic crystal fibers (HC-PCF) [7–18], tapered fibers [19–21] and exposed-core fibers [22]. These optical fiber approaches have been paralleled by work based on chip-based waveguides [23–27] that aim at better stability and scalability although with higher losses than the fiber approaches.

These experimental architectures have led to optical phase shifts of 1 µrad to 300 µrad per photon being demonstrated within rubidium filled hollow-core fiber [11, 13], as well as all-optical switching using chip-based micro-disks [33].

These strong interactions were only obtained because of the use of tightly confined optical modes. However, as we show here, the small transverse scale of the modes leads to an unavoidable loss of interaction strength because of the limited light-atom interaction times within this constrained geometry.

This paper develops the theory to explain the effect of limited light-atom interaction times on the interaction strength and shows that this explains our observations of photon interactions mediated by a confined thermal ensemble of rubidium atoms. Under such conditions, we show the interaction strength does not scale with the beam intensities as might be naively expected. It is important to understand this effect as otherwise a simple scaling of existing experiments can lead to unrealistically strong expectations of interactions.

II. EXPERIMENT

This paper presents measurements of photon-photon interaction in hollow-core fibers with four different core diameters. The properties of the fibers are summarized in Table I with the corresponding scanning electron microscope images shown in Fig. 1. Three of the fibers (Fibers 2−4) have kagome cladding lattice that guides via Inhibited-Coupling (IC) guiding mechanism [32, 34], while the final fiber (Fiber 1) is a photonic bandgap (PBG) guiding HC-PCF and contrasts with the other fibers by its much smaller core diameter [28, 29]. The dispersion and birefringent properties of the fibers were ignored as only a 400 MHz spectral window was observed [35]. Each fiber supported multiple transverse spatial

Fiber	Core Diameter (µm)	Mode Diameter (µm)	Guidance Range (nm)	Fiber Type	Reference
1	10	7.3 ± 1.6	$700 - 850$	19-cell Bandgap	[28, 29]
2	27×37	24.6 ± 2.8	$420 - 1700$	7-cell Hypocycloid kagome	[30, 31]
3	45	32.9 ± 0.6	$600 - 1700$	Single-cell kagome	[32]
4	60	43.9 ± 0.8	$700 - 850$, $1400 - 1700$	19-cell kagome	[32]

TABLE I. A summary of the fibers used. Fiber core diameters were measured from scanning electron microscope images shown in Fig. 1, while mode diameters were simulated using finite elements modeling of the fundamental mode and confirmed with experimental beam divergence measurements. References are provided for similar types of fiber to those used.

modes; however, through careful matching of the input mode to the fundamental guided mode it was possible to ensure that the fundamental mode was predominantly excited. The far-field spatial mode shape showed a Gaussian profile which confirms coupling to the fundamental mode but does not guarantee single mode guidance. We ascertained an accurate estimate of the diameter of the fundamental guided modes by electromagnetic finite element modeling [36], and then confirmed this by measuring the divergence of the fundamental mode exiting the fiber.

Each of the fibers was ∼30 cm in length and mounted on a stainless steel platform that sits inside a vacuum chamber. The vacuum chamber temperature was maintained between 50 °C to 70 °C (measured at the coldest point on the chamber) to create a dense rubidium (Rb) vapor. To verify the fibers possessed a Rb vapor within their core, fluorescence from the Rb D_2 transition, $5S_{1/2} \rightarrow 5P_{3/2}$, was observed scattering light from the guided mode. Fibers 2−4 showed fluorescence and thus a Rb vapor present along their whole length, on the other hand, the smallest fiber (fiber 1), only showed fluorescence near the fiber ends. For the purposes of a valid inter-comparison between fibers, it is important to determine the effective total atomic number in each fiber which was measured via the optical depth of the D_2 transition, [37], see Table III. The optical depth for fibre 4 was assumed to be that of fibre 3 as they were taken under identical conditions.

The photon-photon coupling within the waveguide is mediated by the $5S_{1/2}\,(F{=}2) \rightarrow 5D_{5/2}\,(F'{=}1{-}4)$ two-photon transition of ^{87}Rb [12, 38], a system that has been shown to produce optical phase shifts sufficient for deterministic photon processing [11, 13]. Although the ^{85}Rb isotope would have offered a stronger interaction under given conditions (due to its higher natural abundance), this paper focuses on the ^{87}Rb isotope as its excited state hyperfine splitting is fully resolved. This allows a clearer exposition of the broadening processes.

Figure 2(a) shows the atomic energy levels, driving lasers, and decay routes for the relevant processes used in this experiment. The strength of the two-photon nonlinearity is enhanced by tuning the probe (780 nm) and pump (776 nm) lasers so that the intermediate frequency of the two photon transition is in the environs (≈2.1 GHz red-detuned) of the $5P_{3/2}$ state. The 780 nm and 776 nm lasers enter the fiber from opposite ends to implement a

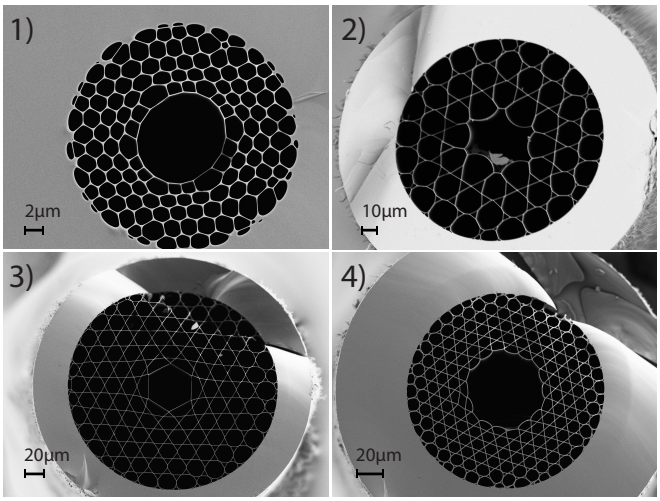

FIG. 1. Scanning electron microscope images of the four different fibers used. Labels correspond to the fiber properties summarized in Table I.

Doppler-free counter-propagating excitation of the transition. This leads to both strong light-atom interaction as well as narrow line-widths [12, 38, 39].

The remainder of this paper will label the ground ($5S_{1/2}$) state $|g\rangle$ while the intermediate ($5P_{3/2}$) and excited ($5D_{5/2}$) energy levels are $|i\rangle$ and $|e\rangle$, respectively, with associated decay rates Γ_i and Γ_e. The frequency detuning from the intermediate state is given by $\Delta_i{=}\omega_{gi}{-}\omega_{780}$, and the two-photon detuning $\Delta_e{=}\omega_{ge}{-}(\omega_{780}{+}\omega_{776})$ where ω_{jk} denotes the $|j\rangle \rightarrow |k\rangle$ transition frequency.

The details of the optical arrangement and the detection scheme are shown in Fig. 2(b). A 780 nm extended cavity diode laser (ECDL) and titanium:sapphire laser tuned to 776 nm were used to excite the two-photon transition. The polarization of the two lasers were aligned orthogonally, allowing their separation using polarizing beam splitters after the fibers. Any unwanted reflected light from the input of the fibers remaining after the polarizing beam splitters was rejected using diffraction gratings.

To measure both the 780 nm absorption and phase-shift induced by the 776 nm beam, two separate 780 nm beams of equal power were coupled into the fibers. These two beams were generated using an acoustic optic modulator (AOM) to give a frequency separation of 160 MHz

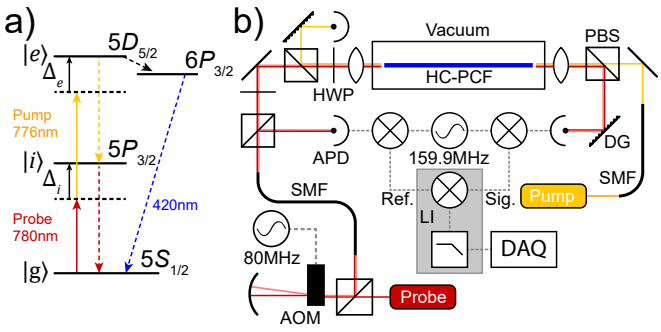

FIG. 2. a) Energy level diagram of the two-photon transition. Solid arrows are driving lasers, dashed arrows show decay routes. b) Schematic of the optical experimental setup. AOM, Acoustic Optic Modulator; SMF, Single mode fiber; PBS, Polarizing beam splitter; HWP, Half wave plate; DG, Diffraction grating; APD, Avalanche Photodiode; PD, Photodiode; LI, Lock-In Amplifier; DAQ, Data Acquisition.

between the two beams (see Fig. 2(b)). This frequency separation is larger than the transition manifold width ≈75 MHz, ensuring that one of the 780 nm beams can act as an unperturbed phase reference, while the second beam can be scanned across the transition to probe the absorption and phase shift. The two 780 nm beams are co-propagating to maximize common-mode rejection of path length fluctuations.

The two 780 nm beams are mixed both before and after the fiber to generate two interference signals Fig. 2(b).We down-mix these interference signals (160 MHz) into the frequency range of a conventional lock-in amplifier using a common local oscillator at 159.9 MHz. The interference signal generated at the input to the fiber is used to synchronize the lock-in amplifier, while the transmission interference signal is synchronously detected by the lock-in amplifier. This measures the complex optical transmittance of the fiber with the high precision and stability of the radio-frequency domain. A typical absorption spectrum of the 780 nm laser is shown in Fig. 3, with each hyperfine absorption feature showing an associated dispersive feature.

For an independent comparison, the two-photon transition was also excited within a conventional Rb cell which was detected through the 420 nm fluorescence generated from the two-photon transition decay, see Fig. 2(a). The input intensity into the cell was adjusted well below the saturation power of the transition to provide a measure of the linewidth of an unsaturated two-photon transition in an unconstrained geometry. The relative optical frequency was derived in a two-step procedure: an optical cavity with a free-spectral range of ∼300 MHz was used to provide a set of equally-separated markers on the frequency axis. The frequency separation and position of these markers was accurately calibrated using the known frequency positions and spacings of the resonant features of the rubidium vapour contained within the cell (see Fig. 3 [38]). Over a frequency range

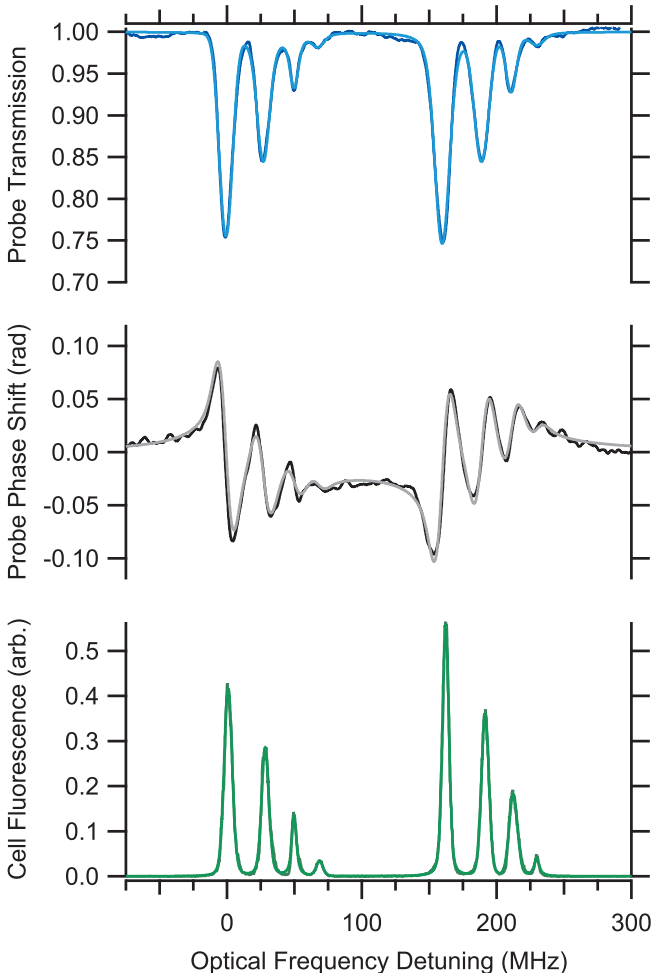

FIG. 3. Example two-photon absorption spectra (top) and phase-shift (middle) recorded on the probe (780 nm) light within the 45 µm core-diameter fiber, Fiber 3. A reference fluorescence spectra from a bulk cell was recorded simultaneously (bottom). In this example P_{780}≈1 µW and P_{776}≈300 µW. Frequency detuning corresponds to probe (780 nm) detuning

of 400 MHz we estimate a maximum frequency axis error of ±570 kHz.

III. RESULTS

To characterize the photon-photon coupling strength, two-photon spectra were taken at a variety of pump and probe powers. The complex response of a Doppler broadened transition can be modeled as a Faddeeva function, defined as $w(z)=e^{z^2}\mathrm{erfc}[-i\,z]$. The real part of the Faddeeva function is the traditional Voigt function (a convolution of a Lorentzian and Gaussian functions) that provides a model of the optical depth of the absorptive media. The imaginary part of the Faddeeva function can be used to model the optical phase-shift caused by a Doppler-broadened absorption. In a typi-

cal free atomic vapor, the Lorentzian component arises from the excited state lifetime (238.5 ns resulting in a 667.3 kHz linewidth [40]). A Gaussian contribution to the linewidth arises from residual Doppler broadening as the two counter-propagating beams are not the same wavelength [39]. This creates a $1/e$ Doppler broadened half-width of ≈1.7 MHz. The limited light-atom interaction time of the atom transiting the optical mode, averaged over all possible trajectories and velocities, leads to a transit-time broadening that increases both the Lorentzian and Gaussian component widths. To measure the transit-time effect on both the optical depth and phase shift as a function of the optical mode size in the various fibers, the complex Faddeeva function was fitted to each of the excited state hyperfine components.

Figure 3 shows the data and fits to the absorption spectra, optical phase shift and cell fluorescence. The absorption and optical phase shift spectra were fitted simultaneously. For each hyperfine transition the position, amplitude, Lorentzian and Gaussian widths are all free parameters to allow for power dependent spectral broadening that effected each of the hyperfine transitions differently. Each of the two absorption and phase-shift spectra for each hyperfine transition share position and width parameters.

The retrieved $5S_{1/2}\,(F{=}2) \rightarrow 5D_{5/2}\,(F'{=}4)$ transition optical depth, phase shift, and spectral linewidth full-width at half-maximum, FWHM, from fitting are presented in Fig. 4 for varying 776 nm powers within the 45 µm-core diameter fiber, Fiber 3. To compare the strength of the two-photon transition within each fiber we use a measure of the optical depth and phase-shift per photon, while the spectral FWHM linewidth within each fiber is presented near zero-power. To measure only the effect of the confined geometries upon the light-atom interactions power dependent broadening was avoided by maintaining the 780 nm probe power below observed two-photon 'saturation' value while measurements were made. It can be seen in Fig. 4, large 776 nm control powers broaden the two-photon transition, lowering the effective photon interaction strength. To extrapolate the two-photon interaction strength to the single-photon regime, a theoretical understanding of the characteristics of the two-photon transition is necessary.

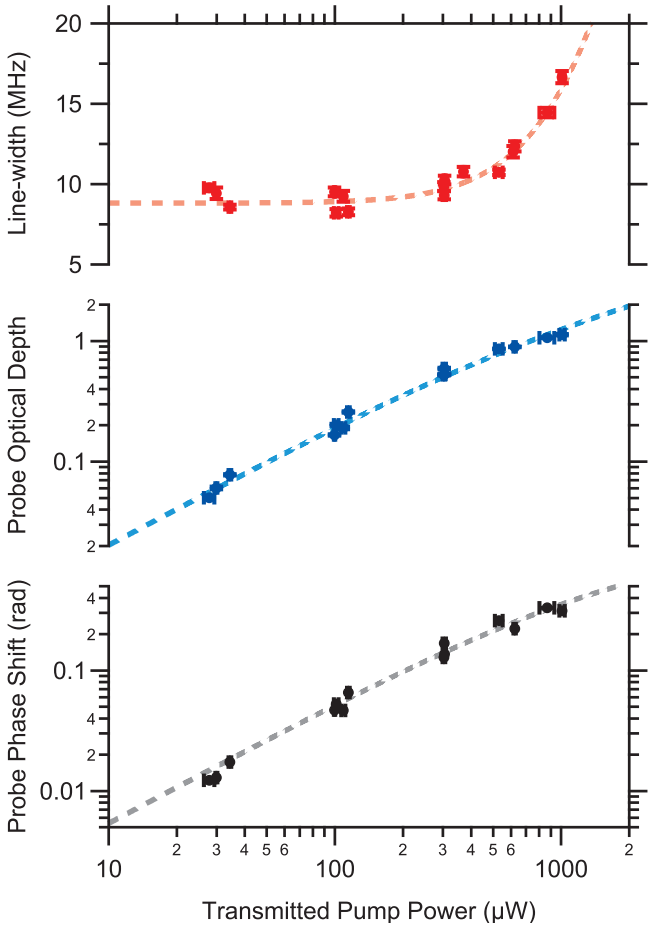

FIG. 4. The two-photon transition's FWHM (top), optical depth (middle), and maximum phase shift (bottom) of the $5S_{1/2}\,(F{=}2) \rightarrow 5D_{5/2}\,(F'{=}4)$ hyperfine transition for the 45 µm core-diameter fiber, Fiber 3. The probe (780 nm) power was below saturation for these measurements while the pump (776 nm) power is changed from below atomic saturation to a regime that shows both power broadening and light shifts. Each data point represents a different combination of probe an pump powers. Error bars represent the standard error of the mean.

IV. THEORY

The two-photon transition was modeled using a five-level atomic model, consisting of two hyper-fine ground states $|g_1\rangle$ and $|g_2\rangle$, an intermediate state $|i\rangle$ and the two-photon excited state $|e\rangle$. From the excited state the atom can decay back to the ground state via the intermediate state $|i\rangle$ or an alternative decay path $|d\rangle$, shown in Fig. 2. The decay rate between any two level $|j\rangle \rightarrow |k\rangle$ is denoted Γ_{jk}. Two lasers excite the two-photon transition coupling the $|g\rangle \rightarrow |i\rangle$ and $|i\rangle \rightarrow |e\rangle$ transitions with coupling strengths Ω_{gi} and Ω_{ie} respectively. In the atomic frame, detuning from the intermediate and two-photon state are expressed as $\Delta_i{=}\omega_{gi}{-}\omega_{780}(1{-}v_z/c)$ and $\Delta_e{=}(\omega_{gi}{+}\omega_{ie}){-}\omega_{780}(1{-}v_z/c){-}\omega_{776}(1{+}v_z/c)$ respectively, see Fig. 2a). The state evolution of a particular atom crossing the optical mode is governed by the optical Bloch master equation. The master equation for the atomic density matrix, ρ, takes the general form:

$$\frac{d\rho(t,x)}{dt} = -i\,[H_0 + H_i(t,x), \rho] + \sum_{j,k} \Gamma_{j,k} \mathcal{D}\,[|j\rangle\,\langle k|]\,\rho \quad (1)$$

A decay rate of $\Gamma_{j,k}$ links states $|j\rangle$ to $|k\rangle$, incorporated into the optical Block equation via the Lindblad superoperator [41]. The total decay from state $|j\rangle$ is denoted Γ_j.

In the absence of external electric and magnetic fields

Parameter	Value	Reference
τ_{5P}	26.24 ns	[42]
τ_{5D}	238.5 ns	[40]
μ_{5P}	$4.227\, e\, a_0$	[37, 42]
μ_{5D}	$0.991\, e\, a_0$	[40, 43]

TABLE II. A summary of the atomic parameters used in the numerical model. The dipole-matrix elements are $\mu_{5P}=\left|\langle 5P_{3/2}|\, er\, |5S_{1/2}\rangle\right|$ and $\mu_{5D}=\left|\langle 5D_{5/2}|\, er\, |5P_{3/2}\rangle\right|$, e is the elementary charge, and a_0 is the Bohr radius.

the atomic Hamiltonian is given by:

$$H_0 = \frac{\omega_{jk}}{2}\left(\sum_k |k\rangle\langle k| - \sum_j |j\rangle\langle j|\right) \tag{2}$$

where ω_{jk} is the transition frequency between states $|j\rangle$ and $|k\rangle$. Finally, the Hamiltonian that governs the light-atom interaction is given by:

$$H_i(t,x) = \sum_{j,k} \Omega_{j,k}(t,x)\left(|j\rangle\langle k| + |k\rangle\langle j|\right) \tag{3}$$

where $\Omega_{j,k}(t,x)$ is the Rabi frequency of the laser coupling the $|j\rangle \rightarrow |k\rangle$ transition which is defined to be $\Omega_{j,k}(t,x)=\mu_{j,k}E_{j,k}(t,x)/\hbar$, where $\mu_{j,k}$ is the dipole matrix element of the transition, see Table II, and $E_{j,k}(t,x)$ is the local electric field coupling the transition.

It is evident in Fig. 4 that power dependent spectral broadening dominates over all other broadening mechanisms at high powers. Thus, to model the power dependent broadening, atomic motion within the HC-PCF was ignored.

Under the experimental conditions, where the 780 nm laser is below saturation $\Omega_{g,i}<\Gamma_i$, it can be assumed that the majority of the population is in the ground state $\rho_{g_1,g_1}+\rho_{g_2,g_2}\approx 1$. Solving Eqns. 1 to 3 for the steady-state coherence observed by the 780 nm probe results in the following:

$$\rho_{g,i} = \frac{-\Omega_{g,i}}{2\Delta_i + i\Gamma_i}\frac{2\left(\Delta_e+\Delta_i\right)+i\Gamma_e}{2\left(\Delta_e+\Delta_i-\frac{\Delta_i\Omega_{i,e}^2}{\Gamma_i^2+4\Delta_i^2}\right)+i\left(\Gamma_e+\frac{\Gamma_i\Omega_{i,e}^2}{\Gamma_i^2+4\Delta_i^2}\right)} \tag{4}$$

The two-photon resonance frequency can be solved for by maximizing the second term giving:

$$\Delta_i \approx \frac{1}{2}\left(\Delta_e \pm \sqrt{\Delta_e^2+\Omega_{i,e}^2}\right) \tag{5}$$

This result shows both Rabi splitting and light-shifts of the two-photon transition frequency for large pump Rabi frequencies $\Omega_{i,e}$. However, it should be noted that power broadening in the traditional sense, associated with population pumping between ground states, is not observed as population transfer through the two-photon transition is relatively minimal. Thus, the broadening of the two-photon transition observed in Fig. 4 is a result of spatially-varying light-shifts of the two-photon transition, Eqn. 5, due to the spatial structure of the optical mode within the HC-PCF.

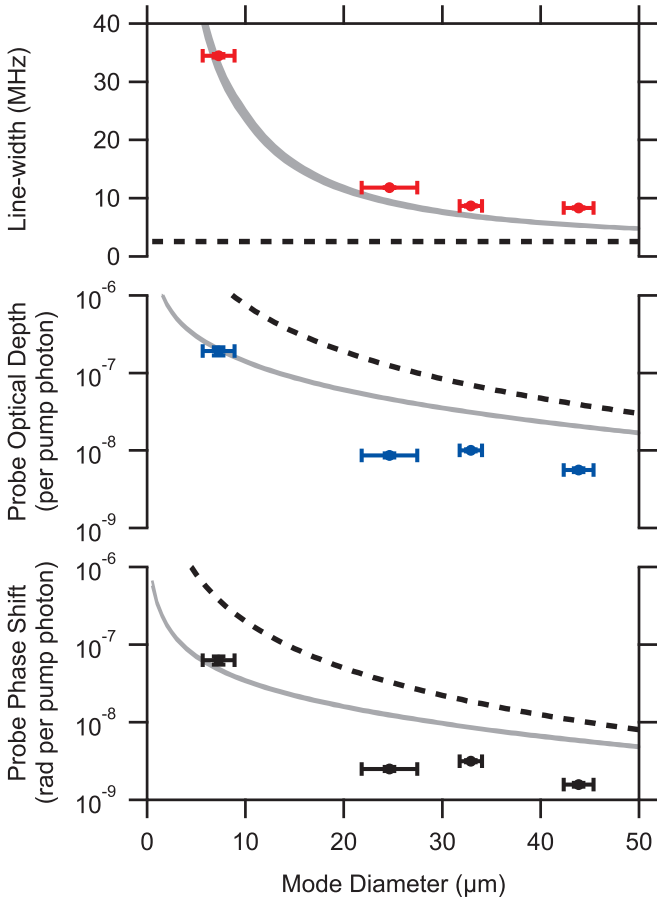

FIG. 5. Spectral line-width FWHM (top), optical depth (middle) and phase shift (bottom) for each fiber characterized in terms of optical mode diameter. The gray bands result from numerical modeling with zero free parameters. Dashed lines represent the numerical modeling result with no transit-time broadening.

To estimate the effect of the light shifts upon the two-photon transition strength, Eqn. 4 was numerically averaged over the spatially-varying light-shifts over the optical mode evaluated for $\Omega_{i,e}<\Delta_e$. The resulting two-photon linshape has a Voigt profile, arising from averaging the Lorentzian two-photon lineshape over a light shift with a Gaussian spatial dependence. The Voigt has a FWHM of:

$$\Gamma\left(\Omega_{i,e}\right) = \Gamma_0\sqrt{1+\left(\Omega_{i,e}/\beta\right)^4} \tag{6}$$

where Γ_0 is the zero-power spectral line-width and β is a saturation parameter. The optical depth and maximum phase-shift per photon similarly take the form:

$$\alpha\left(\Omega_{i,e}\right) = \alpha_0\Omega_{i,e}^2\Gamma_0/\Gamma\left(\Omega_{i,e}\right) \tag{7}$$

$$\Phi\left(\Omega_{i,e}\right) = \Phi_0\Omega_{i,e}^2\Gamma_0/\Gamma\left(\Omega_{i,e}\right) \tag{8}$$

	Measured				Scaled	
Fiber	Rb^{87} Col. Dens. ($10^{15}m^{-2}$)	Line-width (MHz)	Optical Depth per Photon (10^{-9})	Phase Shift per Photon (nrad)	Optical Depth per Photon (10^{-9})	Phase Shift per Photon (nrad)
1	5.5 ± 0.6	34.9 ± 0.5	440 ± 6	146 ± 2	189 ± 22	63 ± 8
2	6.1 ± 0.3	12.1 ± 0.6	22 ± 1	6.4 ± 0.1	8.6 ± 1.0	2.5 ± 0.2
3	2.4 ± 0.04	8.7 ± 0.2	10.1 ± 1.0	3.2 ± 0.1	10.0 ± 1.0	3.2 ± 0.1
4	2.4 ± 0.04	7.8 ± 0.1	5.6 ± 0.3	1.6 ± 0.1	5.6 ± 0.3	1.6 ± 0.1

TABLE III. A summary of the two-photon optical depths and phase shifts observed within the fibers. The three measured columns present the Rb column density, measured using the $5S_{1/2} \rightarrow 5P_{3/2}$, D_2 optical depths, and the two-photon optical depth and phase shift per photon extracted from zero-power extrapolation like that shown in Fig. 4. The two scaled columns, scale each of the fibers Rb column densities to match that of Fiber 4 to clearly show the dependence on optical mode diameter.

where α_0 and Φ_0 are the asymptotic maximum optical depth and phase shift the atomic ensemble can produce due to broadening effects. Equations 6 to 8 were used to extract the zero-power spectral line-width, optical depth and optical phase shift per photon for each fiber from the power dependence data, Fig. 4, the results of which are presented in Fig. 5.

In the limit of single-photon excitation, the dominant broadening mechanism is the limited interaction time between the light and atoms, which is brought about by transit-time broadening. To calculate the effect of transit-time broadening the absorption and phase shift were averaged over all possible trajectories and velocities through the optical mode [44–46]. We averaged the two-photon coherences over all transverse speeds v_t and axial velocities v_z using a Maxwell-Boltzmann distribution. The averaged refractive index was evaluated via:

$$n_{g,i}(\Delta) = 1 + \frac{\bar{\chi}_{g,i}(\Delta)}{2} \tag{9}$$

where $\bar{\chi}_{g,i}(\Delta)$ is the averaged susceptibility which is assumed to be small, following from the low power excitation assumption. The averaged susceptibility is calculated by numerically averaging over the aforementioned physical processes:

$$\bar{\chi}_{g,i}(\Delta) = Nc\hbar \times \frac{\int_0^\infty dv_t \int_{-\infty}^{\infty} dA\, dv_z\, \Omega_{g,i}(y,x)\rho_{g,i}(y,x)F(v_t,v_z)}{\int_{-\infty}^{\infty} dA\, I_{g,i}(y,x)} \tag{10}$$

where dA is the cross-sectional mode area with $dA{=}dx\,dy$, N is the number density of the vapor, c is the speed of light, $\hbar$ is the reduced Planck constant, and $F(v_t,v_z){=}F_t(v_t)F_z(v_z)$ where $F_t(v_t)$ and $F_z(v_z)$ are the axial and transverse Maxwell-Boltzmann velocity distribution functions respectively [46]. It is assumed that the optical phase front remains uniform through the fiber as the phase shift imparted is small, thus lensing effects have been ignored. The optical depth and phase shift where then calculated via $\alpha_{g,i}(\Delta){=}2\omega_{g,i}\,\mathrm{Im}(n_{g,i}(\Delta))/c$ and $\phi_{g,i}(\Delta){=}\omega_{g,i}\,\mathrm{Re}(n_{g,i}(\Delta))/c$ respectively [41].

The modeled spectral lineshape resulting from evaluating Eqn. 9 include: the natural line-shape of the two-photon transition, residual Doppler broadening, and transit-time broadening. The natural line shape of the two-photon transition was incorporated thought the equations of motion Eqn. 1, while residual Doppler broadening results from averaging over all axial velocities, v_z, in Eqn. 10. Transit-time broadening arises from averaging over all transverse velocities, v_t, and trajectories through the optical mode, dx and dy, in Eqn. 10. Finally, the resultant modeled lineshape was convolved with the 780 nm and 776 nm lasers linewidths, measured to both be 1.1 MHz, integrated over the time to acquire a single spectra.

The result of the modeling is shown by the gray lines on Fig. 5 showing good agreement with the experimental data. It is important to note that there are no free parameters in this modeling with all atomic parameters such as decay rate and transition dipole matrix elements being taken from the literature (see Table II), while all the experimental parameters, such as the length of the fiber, were measured and fixed in the analysis. The largest uncertainty was knowledge of the 780 nm and 776 nm laser spatial mode overlap along the length of the fibers. Mismatch of the spatial optical modes would greatly reduce the two-photon excitation efficiency, which is proportional to the product of the laser intensities, within the highly multi-mode fibers (fibers 2−4) which is seen in the experimental data.

V. DISCUSSION

The extrapolated zero-power spectral line-width FWHM for each fiber are presented in Fig. 5 (top), characterised in terms of optical mode diameter, along with the numerical modeling. We have included (not included) the effects of transit-time broadening in the modeling in the grey (dashed) lines. The vertical error bars are extracted from uncertainty in extrapolation to zero-power, while horizontal error bars follow from Table I. The data shows good agreement with numerical modeling.

With decreasing mode diameters, the two-photon linewidths show a clear departure from the linewidths expected from the natural linewidth and residual Doppler broadening. This departure is a result of the limited light-atom interaction time. As the interaction time is proportional to the mode diameters, d, the transit time broadening is proportional to $1/d$, as depicted by the

dotted line in Fig. 5 (top). In the most extreme example, Fiber 1, the mode diameter of (7.3 ± 1.6) µm leads to a transit-time of atoms through the optical mode, averaged over all velocities and trajectories, of ≈33 ns. This is substantially smaller than the natural lifetime of the excited state, 238.5 ns [40], leading to a spectral FWHM of (34.9 ± 0.5) MHz dominated by transit-time spectral broadening.

The optical depth and phase shift generated per input photon for each of the different fiber core diameters is also shown in bottom two panels of Fig. 5 respectively. In each case, these values have been scaled to the Rb absorption present in Fiber 4 so that it is easy to make a comparison between different mode diameters, see Table III. Typically the two-photon interaction strength is proportional to the pump beams intensity, thus $1/d^2$. However, as a result of the transit-time broadened spectral line-width, the dependence of both the optical depth and phase shift per photon upon mode diameter is reduced to $1/d$. This is also evident in the numerical modeling where we have alternatively included or excluded the effects of transit-time broadening (see the grey and black dashed lines in Fig. 5 respectively). The experimentally measured optical depth and phase shift follow the general trend of the theoretical model, gray line, indicating the changing mode radius and finite light-atom interaction time explain the observed photon-photon interaction strength. The deviation between experiment and modeling in some cases may be due to poor determination of the Rb vapor column density within the fibers.

It is clear that the effect of transit-time broadening profoundly influences the strength of the light-atom coupling and thus the photon-photon interaction strength. This has significant implications for waveguide-based platforms that intend to use warm vapors to mediate such interactions rendering them less efficient than might be expected if the effects of transit-time broadening are ignored.

To maximize the interaction strength between two photons this analysis points a way forward: one needs to simultaneously use a constrained geometry to maximize the intensity of the light while also setting the coherent interaction time between the atoms and light to be at least equal to the lifetime of the excited atomic energy level. If the nonlinear effect is mediated by ground-state transitions, also affected by transit-time broadening, then the coherence could be increased by using a buffer-gas [47, 48] or by applying an anti-relaxation coating to the fiber core walls [49, 50], relevant to quantum optical memory applications [15]. These techniques, however, do not extend the coherent interaction time with an optically excited state: in this case one requires no collisions with other atoms or the fiber wall. One solution to extend excited state coherence is to reduce the average motion of the atoms, pointing towards laser-cooled atoms as a route to create strong photon-photon interaction mediated by light-atom interactions in waveguide geometries [8, 19, 35, 51, 52].

VI. CONCLUSION

We have presented a broad study into photon-photon interactions mediated via a rubidium vapor loaded within hollow-core fibers with a range of different core sizes. We show limited light-atom interaction time leads to transit-time broadening, increasing the spectral line-width proportional to $1/d$. As a result, the interaction strength increases proportional to the optical mode diameter, $1/d$, rather than that typically expected from an increasing intensity field, $1/d^2$. The optical depth and phase shift induced upon one optical mode as a result of the magnitude of the second optical mode was shown to agree well with a derived theoretical model of the two-photon transition. As a result, this work allows accurate estimation of the expected photon-photon interaction strength to be expected from a given waveguide geometry, thus allowing waveguides to be designed to target specific photon-photon interaction strengths.

FUNDING INFORMATION

The authors acknowledge financial support from the Australian Research Council under grants DP0877938, DE120102028, and FT0991631. This research was supported by the South Australian Government through the Premier's Science and Research Fund.

ACKNOWLEDGMENTS

We are grateful to Francois Couny for his contribution in the fiber fabrication the HC-PCF, and A. G. White for his stimulating discussions and guidance. We acknowledge the Australian Microscopy and Microanalysis Research Facility at the University of Western Australia, a facility funded by the university and state and commonwealth governments.

[1] P. Kok, K. Nemoto, T. C. Ralph, J. P. Dowling, and G. J. Milburn, "Linear optical quantum computing with photonic qubits," Reviews of Modern Physics **79**, 135–174 (2007).

[2] H. J. Kimble, "The quantum internet." Nature **453**, 1023–30 (2008).

[3] K. Hammerer, A. S. Sørensen, and E. S. Polzik, "Quantum interface between light and atomic ensembles," Reviews of Modern Physics **82**, 1041–1093 (2010).

[4] K. Nemoto and W. J. Munro, "Nearly deterministic linear optical controlled-NOT gate," Physical Review Letters **93**, 250502 (2004).

[5] W. J. Munro, K. Nemoto, and T. P. Spiller, "Weak nonlinearities: A new route to optical quantum computation," New Journal of Physics **7** (2005).

[6] S. D. Barrett, P. Kok, K. Nemoto, R. G. Beausoleil, W. J. Munro, and T. P. Spiller, "Symmetry analyzer for nondestructive Bell-state detection using weak nonlinearities," Physical Review A - Atomic, Molecular, and Optical Physics **71**, 2–5 (2005).

[7] P. Londero, V. Venkataraman, A. Bhagwat, A. Slepkov, and A. L. Gaeta, "Ultralow-Power Four-Wave Mixing with Rb in a Hollow-Core Photonic Band-Gap Fiber," Physical Review Letters **103**, 043602 (2009).

[8] M. Bajcsy, S. Hofferberth, V. Balic, T. Peyronel, M. Hafezi, A. S. Zibrov, V. Vuletic, and M. D. Lukin, "Efficient All-Optical Switching Using Slow Light within a Hollow Fiber," Phys Rev Lett **102**, 203902 (2009).

[9] M. Bajcsy, S. Hofferberth, T. Peyronel, V. Balic, Q. Liang, A. S. Zibrov, V. Vuletic, and M. D. Lukin, "Laser-cooled atoms inside a hollow-core photonic-crystal fiber," Phys Rev A **83**, 063830 (2011).

[10] V. Venkataraman, K. Saha, P. Londero, and A. L. Gaeta, "Few-Photon All-Optical Modulation in a Photonic Band-Gap Fiber," Phys Rev Lett **107**, 193902 (2011).

[11] V. Venkataraman, K. Saha, and A. L. Gaeta, "Phase modulation at the few-photon level for weak-nonlinearity-based quantum computing," Nat Photonics **7**, 5–8 (2013).

[12] C. Perrella, P. S. Light, J. D. Anstie, T. M. Stace, F. Benabid, and A. N. Luiten, "High-Resolution Two-Photon Spectroscopy of Rubidium within Confined Geometry," Phys Rev A **87**, 013818 (2013).

[13] C. Perrella, P. S. Light, J. D. Anstie, F. Benabid, T. M. Stace, A. G. White, and A. N. Luiten, "High-efficiency cross-phase modulation in a gas-filled waveguide," Phys Rev A **88**, 013819 (2013).

[14] M. R. Sprague, D. G. England, A. Abdolvand, J. Nunn, X.-M. Jin, W. Steven Kolthammer, M. Barbieri, B. Rigal, P. S. Michelberger, T. F. M. Champion, P. S. J. Russell, and I. A. Walmsley, "Efficient optical pumping and high optical depth in a hollow-core photonic-crystal fibre for a broadband quantum memory," New Journal of Physics **15**, 055013 (2013).

[15] M. R. Sprague, P. S. Michelberger, T. F. M. Champion, D. G. England, J. Nunn, X.-M. Jin, W. S. Kolthammer, A. Abdolvand, P. S. J. Russell, and I. A. Walmsley, "Broadband single-photon-level memory in a hollow-core photonic crystal fibre," Nat Photonics **8**, 287–291 (2014).

[16] G. Epple, K. S. Kleinbach, T. G. Euser, N. Y. Joly, T. Pfau, P. S. J. Russell, and R. Löw, "Rydberg atoms in hollow-core photonic crystal fibres." Nat Commun **5**, 4132 (2014).

[17] P. S. Donvalkar, V. Venkataraman, S. Clemmen, K. Saha, and A. L. Gaeta, "Frequency translation via four-wave mixing Bragg scattering in Rb filled photonic bandgap fibers," Optics Letters **39**, 1557 (2014).

[18] T. D. Bradley, E. Ilinova, J. J. McFerran, J. Jouin, B. Debord, M. Alharbi, P. Thomas, F. Gérôme, and F. Benabid, "Ground-state atomic polarization relaxation-time measurement of Rb filled hypocycloidal core-shaped Kagome HC-PCF," Journal of Physics B: Atomic, Molecular and Optical Physics **49**, 185401 (2016).

[19] E. Vetsch, D. Reitz, G. Sagué, R. Schmidt, S. T. Dawkins, and A. Rauschenbeutel, "Optical Interface Created by Laser-Cooled Atoms Trapped in the Evanescent Field Surrounding an Optical Nanofiber," Phys Rev Lett **104**, 203603 (2010).

[20] S. M. Hendrickson, M. M. Lai, T. B. Pittman, and J. D. Franson, "Observation of Two-Photon Absorption at Low Power Levels Using Tapered Optical Fibers in Rubidium Vapor," Phys Rev Lett **105**, 173602 (2010).

[21] A. Goban, K. S. Choi, D. J. Alton, D. Ding, C. Lacroûte, M. Pototschnig, T. Thiele, N. P. Stern, and H. J. Kimble, "Demonstration of a State-Insensitive, Compensated Nanofiber Trap," Phys Rev Lett **109**, 033603 (2012).

[22] C. Perrella, H. P. Griesser, P. S. Light, R. Kostecki, T. M. Stace, H. Ebendorff-Heidepriem, T. M. Monro, A. G. White, and A. N. Luiten, "Demonstration of Exposed Core Fibre Platform for Two-Photon Rubidium Spectroscopy," Phys Rev Applied **4**, 014013 (2015).

[23] W. Yang, D. B. Conkey, B. Wu, D. Yin, A. R. Hawkins, and H. Schmidt, "Atomic spectroscopy on a chip," Nat Photonics **1**, 331–335 (2007).

[24] B. Wu, J. F. Hulbert, E. J. Lunt, K. Hurd, A. R. Hawkins, and H. Schmidt, "Slow light on a chip via atomic quantum state control," Nature Photonics **4**, 776–779 (2010).

[25] L. Stern, B. Desiatov, I. Goykhman, and U. Levy, "Nanoscale light-matter interactions in atomic cladding waveguides." Nat Commun **4**, 1548 (2013).

[26] L. Stern, B. Desiatov, N. Mazurski, and U. Levy, "Strong coupling and high-contrast all-optical modulation in atomic cladding waveguides," Nature Communications **8**, 14461 (2017).

[27] P. Sibson, J. E. Kennard, S. Stanisic, C. Erven, J. L. O'Brien, and M. G. Thompson, "Integrated silicon photonics for high-speed quantum key distribution," Optica **4**, 172 (2017).

[28] P. Russell, "Photonic crystal fibers." Science (New York, N.Y.) **299**, 358–62 (2003).

[29] G. Bouwmans, F. Luan, J. Knight, P. St. J. Russell, L. Farr, B. Mangan, and H. Sabert, "Properties of a hollow-core photonic bandgap fiber at 850 nm wavelength," Optics Express **11**, 1613 (2003).

[30] Y. Y. Wang, N. V. Wheeler, F. Couny, P. J. Roberts, and F. Benabid, "Low loss broadband transmission in hypocycloid-core Kagome hollow-core photonic crystal fiber." Optics letters **36**, 669–671 (2011).

[31] T. D. Bradley, Y. Wang, M. Alharbi, B. Debord, C. Fourcade-Dutin, B. Beaudou, F. Gerome, and F. Benabid, "Optical Properties of Low Loss (70dB/km) Hypocycloid-CoreKagome Hollow Core Photonic Crystal Fiber for Rb and Cs BasedOptical Applications," Journal of Lightwave Technology **31**, 2752–2755 (2013).

[32] F. Couny, F. Benabid, and P. S. Light, "Large-pitch kagome-structured hollow-core photonic crystal fiber." Optics letters **31**, 3574–3576 (2006).

[33] S. M. Hendrickson, C. N. Weiler, R. M. Camacho, P. T. Rakich, A. I. Young, M. J. Shaw, T. B. Pittman, J. D. Franson, and B. C. Jacobs, "All-optical-switching demonstration using two-photon absorption and the Zeno effect," Phys Rev A **87**, 023808 (2013).

[34] F. Couny, F. Benabid, P. J. Roberts, P. S. Light, M. G. Raymer, O.-F. Combs, F. Couny, F. Benabid, P. J. Roberts, P. S. Light, and M. G. Raymer, "Generation

and Photonic," Science **318**, 1118–1121 (2007).

[35] S. Okaba, T. Takano, F. Benabid, T. Bradley, L. Vincetti, Z. Maizelis, V. Yampol'skii, F. Nori, and H. Katori, "Lamb-Dicke spectroscopy of atoms in a hollow-core photonic crystal fibre," Nature Communications **5**, 4096 (2014).

[36] E. N. Fokoua, S. R. Sandoghchi, Y. Chen, T. Jasion, N. V. Wheeler, N. K. Baddela, J. R. Hayes, M. N. Petrovich, D. J. Richardson, and F. Poletti, "Accurate modelling of fabricated hollow-core photonic bandgap fibers," **23**, 20980–20991 (2015).

[37] P. Siddons, C. S. Adams, C. Ge, and I. G. Hughes, "Absolute absorption on rubidium D lines: comparison between theory and experiment," Journal of Physics B: Atomic, Molecular and Optical Physics **41**, 155004 (2008).

[38] F. Nez, F. Biraben, R. Felder, and Y. Millerioux, "Optical frequency determination of the hyperfine components of the two-photon transitions in rubidium," Optics Communications **102**, 432–438 (1993).

[39] J. Bjorkholm and P. Liao, "Line shape and strength of two-photon absorption in an atomic vapor with a resonant or nearly resonant intermediate state," Phys Rev A **14**, 751–760 (1976).

[40] D. Sheng, A. Pérez Galván, and L. A. Orozco, "Lifetime measurements of the 5d states of rubidium," Phys Rev A **78**, 062506 (2008).

[41] R. Loudon, *The Quantum Theory Of Light* (Oxford University Press, New York, 2001), 3rd ed.

[42] D. A. Steck, "Rubidium 87 D line data," `http://steck.us/alkalidata`. (revision 2.1.4, 23 December 2010).

[43] M. Safronova and U. Safronova, "Critically evaluated theoretical energies, lifetimes, hyperfine constants, and multipole polarizabilities in ˆ{87}Rb," Physical Review A **83**, 052508 (2011).

[44] C. J. Bordé, J. L. J. Hall, C. V. Kunasz, and D. G. D. Hummer, "Saturated absorption line shape: Calculation of the transit-time broadening by a perturbation approach," Physical Review A **14**, 236–263 (1976).

[45] S. N. Bagayev, V. P. Chebotayev, and E. A. Titov, "Saturated absorption lineshape under the transit-time conditions," Laser Phys **4**, 224–292 (1994).

[46] T. M. Stace and A. N. Luiten, "Theory of spectroscopy in an optically pumped effusive vapor," Phys Rev A **81**, 033848 (2010).

[47] M. D. Lukin, M. Fleischhauer, A. S. Zibrov, H. G. Robinson, V. L. Velichansky, L. Hollberg, and M. O. Scully, "Spectroscopy in Dense Coherent Media: Line Narrowing and Interference Effects," Physical Review Letters **79**, 2959–2962 (1997).

[48] A. Javan, O. Kocharovskaya, H. Lee, and M. O. Scully, "Narrowing of electromagnetically induced transparency resonance in a Doppler-broadened medium," Physical Review A **66**, 013805 (2002).

[49] P. S. Light, F. Benabid, F. Couny, M. Maric, and A. N. Luiten, "Electromagnetically induced transparency in Rb-filled coated hollow-core photonic crystal fiber," Optics Letters **32**, 1323 (2007).

[50] Y. W. Yi, H. G. Robinson, S. Knappe, J. E. Maclennan, C. D. Jones, C. Zhu, N. A. Clark, and J. Kitching, "Method for characterizing self-assembled monolayers as antirelaxation wall coatings for alkali vapor cells," Journal of Applied Physics **104**, 023534 (2008).

[51] G. Sagué, E. Vetsch, W. Alt, D. Meschede, and A. Rauschenbeutel, "Cold-Atom Physics Using Ultrathin Optical Fibers: Light-Induced Dipole Forces and Surface Interactions," Physical Review Letters **99**, 163602 (2007).

[52] J. Poulin, P. S. Light, R. Kashyap, and A. N. Luiten, "Optimized coupling of cold atoms into a fiber using a blue-detuned hollow-beam funnel," Physical Review A **84**, 053812 (2011).